



Full Length Article

Method to measure muon content of extensive air showers with LHAASO KM2A-WCDA synergy[☆]

Zhen Cao¹, F. Aharonian^{4,5}, Q. An^{6,7}, Axikegu⁸, L.X. Bai⁹, Y.X. Bai^{1,3}, Y.W. Bao¹⁰, D. Bastieri¹¹, X.J. Bi^{1,2,3}, Y.J. Bi^{1,3}, J.T. Cai¹¹, Q. Cao¹², W.Y. Cao⁷, Zhe Cao^{6,7}, J. Chang¹³, J.F. Chang^{1,3,6}, E.S. Chen^{1,2,3}, Liang Chen¹³, Lin Chen⁸, Long Chen⁸, M.J. Chen^{1,3}, M.L. Chen^{1,3,6}, Q.H. Chen⁸, S.H. Chen^{1,2,3}, S.Z. Chen^{1,3}, T.L. Chen¹⁴, Y. Chen¹⁰, H.L. Cheng^{2,15,14}, N. Cheng^{1,3}, Y.D. Cheng^{1,3}, S.W. Cui¹², X.H. Cui¹⁵, Y.D. Cui¹⁶, B.Z. Dai¹⁷, H.L. Dai^{1,3,6}, Z.G. Dai⁷, Danzengluobu¹⁴, D. della Volpe¹⁸, X.Q. Dong^{1,2,3}, K.K. Duan¹³, J.H. Fan¹¹, Y.Z. Fan¹³, J. Fang¹⁷, K. Fang^{1,3}, C.F. Feng¹⁹, L. Feng¹³, S.H. Feng^{1,3}, X.T. Feng¹⁹, Y.L. Feng¹⁴, B. Gao^{1,3}, C.D. Gao¹⁹, L.Q. Gao^{1,2,3}, Q. Gao¹⁴, W. Gao^{1,3}, W.K. Gao^{1,2,3}, M.M. Ge¹⁷, L.S. Geng^{1,3}, G.H. Gong²⁰, Q.B. Gou^{1,3}, M.H. Gu^{1,3,6}, F.L. Guo¹³, X.L. Guo⁸, Y.Q. Guo^{1,3}, Y.Y. Guo¹³, Y.A. Han²¹, H.H. He^{1,2,3}, H.N. He¹³, J.Y. He¹³, X.B. He¹⁶, Y. He⁸, M. Heller¹⁸, Y.K. Hor¹⁶, B.W. Hou^{1,2,3}, C. Hou^{1,3}, X. Hou²², H.B. Hu^{1,2,3}, Q. Hu^{7,13}, S.C. Hu^{1,2,3}, D.H. Huang⁸, T.Q. Huang^{1,3}, W.J. Huang¹⁶, X.T. Huang¹⁹, X.Y. Huang¹³, Y. Huang^{1,2,3}, Z.C. Huang⁸, X.L. Ji^{1,3,6}, H.Y. Jia⁸, K. Jia¹⁹, K. Jiang^{6,7}, X.W. Jiang^{1,3}, Z.J. Jiang¹⁷, M. Jin⁸, M.M. Kang⁹, T. Ke^{1,3}, D. Kuleshov²³, K. Kurinov²³, B.B. Li¹², Cheng Li^{6,7}, Cong Li^{1,3}, D. Li^{1,2,3}, F. Li^{1,3,6}, H.B. Li^{1,3}, H.C. Li^{1,3}, H.Y. Li^{7,13}, J. Li^{7,13}, Jian Li⁷, Jie Li^{1,3,6}, K. Li^{1,3}, W.L. Li¹⁹, W.L. Li²⁴, X.R. Li^{1,3}, Xin Li^{6,7}, Y.Z. Li^{1,2,3}, Zhe Li^{1,3}, Zhuo Li²⁵, E.W. Liang²⁶, Y.F. Liang²⁶, S.J. Lin¹⁶, B. Liu⁷, C. Liu^{1,3}, D. Liu¹⁹, H. Liu⁸, H.D. Liu²¹, J. Liu^{1,3}, J.L. Liu^{1,3}, J.L. Liu²⁴, J.S. Liu¹⁶, J.Y. Liu^{1,3}, M.Y. Liu¹⁴, R.Y. Liu¹⁰, S.M. Liu⁸, W. Liu^{1,3}, Y. Liu¹¹, Y.N. Liu²⁰, W.J. Long⁸, R. Lu¹⁷, Q. Luo¹⁶, H.K. Lv^{1,3}, B.Q. Ma²⁵, L.L. Ma^{1,3}, X.H. Ma^{1,3}, J.R. Mao²², Z. Min^{1,3}, W. Mitthumsiri²⁷, Y.C. Nan^{1,3}, Z.W. Ou¹⁶, B.Y. Pang⁸, P. Pattarakijwanich²⁷, Z.Y. Pei¹¹, M.Y. Qi^{1,3}, Y.Q. Qi¹², B.Q. Qiao^{1,3}, J.J. Qin⁷, D. Ruffolo²⁷, A. Sáiz²⁷, C.Y. Shao¹⁶, L. Shao¹², O. Shchegolev^{23,28}, X.D. Sheng^{1,3}, H.C. Song²⁵, Yu.V. Stenkin^{23,28}, V. Stepanov²³, Y. Su¹³, Q.N. Sun⁸, X.N. Sun²⁶, Z.B. Sun²⁹, P.H.T. Tam¹⁶, Z.B. Tang^{6,7}, W.W. Tian^{2,15}, C. Wang²⁹, C.B. Wang⁸, G.W. Wang⁷, H.G. Wang¹¹, H.H. Wang¹⁶, J.C. Wang²², J.S. Wang²⁴, K. Wang¹⁰, L.P. Wang¹⁹, L.Y. Wang^{1,3}, P.H. Wang⁸, R. Wang¹⁹, W. Wang¹⁶, X.G. Wang²⁶, X.Y. Wang¹⁰, Y. Wang⁸, Y.D. Wang^{1,3}, Y.J. Wang^{1,3}, Z.H. Wang⁹, Z.X. Wang¹⁷, Zhen Wang²⁴, Zheng Wang^{1,3,6}, D.M. Wei¹³, J.J. Wei¹³, Y.J. Wei^{1,2,3}, T. Wen¹⁷, C.Y. Wu^{1,3}, H.R. Wu^{1,3}, S. Wu^{1,3}, X.F. Wu¹³, Y.S. Wu⁷, S.Q. Xi^{1,3}, J. Xia^{7,13}, J.J. Xia⁸, G.M. Xiang^{2,13}, D.X. Xiao¹², G. Xiao^{1,3}, G.G. Xin^{1,3}, Y.L. Xin⁸, Y. Xing¹³, Z. Xiong^{1,2,3,*}, D.L. Xu²⁴, R.F. Xu^{1,2,3}, R.X. Xu²⁵, L. Xue¹⁹, D.H. Yan¹⁷, J.Z. Yan¹³, T. Yan^{1,3}, C.W. Yang⁹, F. Yang¹², F.F. Yang^{1,3,6}, H.W. Yang¹⁶, J.Y. Yang¹⁶, L.L. Yang¹⁶, M.J. Yang^{1,3}, R.Z. Yang⁷, S.B. Yang¹⁷, Y.H. Yao⁹, Z.G. Yao^{1,3}, Y.M. Ye²⁰, L.Q. Yin^{1,3}, N. Yin¹⁹, X.H. You^{1,3}, Z.Y. You^{1,2,3}, Y.H. Yu⁷, Q. Yuan¹³, H. Yue^{1,2,3}, H.D. Zeng¹³, T.X. Zeng^{1,3,6}, W. Zeng¹⁷, Z.K. Zeng^{1,2,3}, M. Zha^{1,3}, B.B. Zhang¹⁰, F. Zhang⁸, H.M. Zhang¹⁰, H.Y. Zhang^{1,3}, J.L. Zhang¹⁵,

[☆] LHAASO Collaboration.

* Corresponding author at: Key Laboratory of Particle Astrophysics & Experimental Physics Division & Computing Center, Institute of High Energy Physics, Beijing, 100049, China.

E-mail addresses: hkh@ihep.ac.cn (H.H. He), wusha@ihep.ac.cn (S. Wu), xiongzhen@ihep.ac.cn (Z. Xiong).

<https://doi.org/10.1016/j.nima.2023.168958>

Received 18 June 2023; Received in revised form 12 November 2023; Accepted 22 November 2023

Available online 27 November 2023

0168-9002/© 2023 Elsevier B.V. All rights reserved.

L.X. Zhang¹¹, Li Zhang¹⁷, P.F. Zhang¹⁷, P.P. Zhang^{7,13}, R. Zhang^{7,13}, S.B. Zhang^{2,15},
S.R. Zhang¹², S.S. Zhang^{1,3}, X. Zhang¹⁰, X.P. Zhang^{1,3}, Y.F. Zhang⁸, Yi Zhang^{1,13},
Yong Zhang^{1,3}, B. Zhao⁸, J. Zhao^{1,3}, L. Zhao^{6,7}, L.Z. Zhao¹², S.P. Zhao^{13,19}, F. Zheng²⁹,
Y. Zheng⁸, B. Zhou^{1,3}, H. Zhou²⁴, J.N. Zhou¹³, P. Zhou¹⁰, R. Zhou⁹, X.X. Zhou⁸, C.G. Zhu¹⁹,
F.R. Zhu⁸, H. Zhu¹⁵, K.J. Zhu^{1,2,3,6}, X. Zuo^{1,3}

¹ Key Laboratory of Particle Astrophysics & Experimental Physics Division & Computing Center, Institute of High Energy Physics, Beijing, 100049, China

² University of Chinese Academy of Sciences, Beijing, 100049, China

³ TIANFU Cosmic Ray Research Center, Chengdu, Sichuan, China

⁴ Dublin Institute for Advanced Studies, 31 Fitzwilliam Place, 2 Dublin, Ireland

⁵ Max-Planck-Institut für Nuclear Physics, P.O. Box 103980, Heidelberg, 69029, Germany

⁶ State Key Laboratory of Particle Detection and Electronics, China

⁷ University of Science and Technology of China, Hefei, 230026, Anhui, China

⁸ School of Physical Science and Technology & School of Information Science and Technology, Southwest Jiaotong University, Chengdu, 610031, Sichuan, China

⁹ College of Physics, Sichuan University, Chengdu, 610065, Sichuan, China

¹⁰ School of Astronomy and Space Science, Nanjing University, Nanjing, 210023, Jiangsu, China

¹¹ Center for Astrophysics, Guangzhou University, Guangzhou, 510006, Guangdong, China

¹² Hebei Normal University, Shijiazhuang, 050024, Hebei, China

¹³ Key Laboratory of Dark Matter and Space Astronomy & Key Laboratory of Radio Astronomy, Purple Mountain Observatory, Chinese Academy of Sciences, Nanjing, 210023, Jiangsu, China

¹⁴ Key Laboratory of Cosmic Rays (Tibet University), Ministry of Education, Lhasa, 850000, Tibet, China

¹⁵ National Astronomical Observatories, Chinese Academy of Sciences, Beijing, 100101, China

¹⁶ School of Physics and Astronomy (Zhuhai) & School of Physics (Guangzhou) & Sino-French Institute of Nuclear Engineering and Technology (Zhuhai), Sun Yat-sen University, 519000 Zhuhai & 510275 Guangzhou, Guangdong, China

¹⁷ School of Physics and Astronomy, Yunnan University, Kunming, 650091, Yunnan, China

¹⁸ Département de Physique Nucléaire et Corpusculaire, Faculté de Sciences, Université de Genève, 24 Quai Ernest Ansermet, 1211 Geneva, Switzerland

¹⁹ Institute of Frontier and Interdisciplinary Science, Shandong University, Qingdao, 266237, Shandong, China

²⁰ Department of Engineering Physics, Tsinghua University, Beijing, 100084, China

²¹ School of Physics and Microelectronics, Zhengzhou University, Zhengzhou, 450001, Henan, China

²² Yunnan Observatories, Chinese Academy of Sciences, Kunming, 650216, Yunnan, China

²³ Institute for Nuclear Research of Russian Academy of Sciences, Moscow, 117312, Russia

²⁴ Tsung-Dao Lee Institute & School of Physics and Astronomy, Shanghai Jiao Tong University, Shanghai, 200240, China

²⁵ School of Physics, Peking University, Beijing, 100871, China

²⁶ School of Physical Science and Technology, Guangxi University, Nanning, 530004, Guangxi, China

²⁷ Department of Physics, Faculty of Science, Mahidol University, Bangkok, 10400, Thailand

²⁸ Moscow Institute of Physics and Technology, Moscow, 141700, Russia

²⁹ National Space Science Center, Chinese Academy of Sciences, Beijing, 100190, China

ARTICLE INFO

Keywords:

Muon measurement
Water Cherenkov Detector
LHAASO

ABSTRACT

The measurement of shower muons on an event-by-event basis offers a potent tool for conducting ground-based experiments on gamma rays and cosmic rays due to its sensitivity to primary mass and interaction models. In recent years, underground water Cherenkov detectors as large-area muon counters provide the most powerful way of rejecting cosmic ray background when searching for TeV–PeV gamma rays and cosmic ray electrons, an unprecedented rejection power of 10^4 – 10^5 is achieved. Unburied water Cherenkov detectors are widely used in ground-based gamma astronomy experiments, e.g. Milagro, HAWC, LHAASO-WCDA, etc. However, due to the presence of electromagnetic components, their deployment as event-by-event muon counters has encountered considerable challenges. All the experiments mentioned above reconstruct lateral-distribution-function related parameters to tell a gamma from hadrons. In this work, we first developed a method to utilize the WCDA, to specify muon content in each shower with LHAASO KM2A-WCDA synergy and help LHAASO to gain approximately a 37,650-meter-square effective area as a muon counter.

1. Introduction

Ground-based extensive air showers (EAS) experiments are major facilities for measuring cosmic-ray nuclei with energies over 100 TeV, primary gamma rays with energies over 100 GeV, and cosmic-ray electrons/positrons with energies over 1 TeV [1,2]. The majority of cosmic rays, primarily comprising cosmic-ray protons and other nuclei, interact with atmospheric nuclei, giving rise to both charged and neutral mesons. The former lead to hadronic sub-cascades or decay into muons, while the latter decay into gamma rays which cause electromagnetic sub-cascades. Hadronic showers, in contrast to purely electromagnetic ones, are dominated significantly more strongly by fluctuations in the initial nuclear interactions and have a wider lateral distribution of secondaries. Regardless of the nature of the primary particles, gamma rays and electrons/positrons predominantly constitute the secondary particles observed at ground level. EAS experiments

measure these secondary particles, including the primary cosmic ray's energy, direction, and core position. However, electromagnetic components lack sensitivity to the primary mass and are ineffective at distinguishing between types of primary particles. In contrast, the muon content within EAS offers sensitivity to both primary mass and energy, in accordance with the *Mathew–Heitler model* [3,4]. Heavier nuclei tend to yield more muons and exhibit reduced relative fluctuations in the muon count (N_μ) compared to lighter nuclei at a given primary energy. Consequently, the muon content provides valuable insights for conducting mass composition analyses and for discriminating primary gamma rays or cosmic-ray electrons from cosmic-ray nuclei [5,6].

In recent years, many EAS arrays have attempted to utilize the Cherenkov technique for effective muon content measurement. The Milagro experiment [7] adopted a dual-layer PMT array design in a 4800-meter-square area and 7.5-meter-depth water pond. The utilization of deep water as an absorptive material enabled the top-layer PMTs to efficiently detect the electromagnetic components of EAS, while the bottom-layer PMTs exhibited heightened sensitivity to muon components. This design was anticipated to enhance background

rejection [8]. The HAWC experiment [9], the successor of Milagro, comprised a 300-unit array of water Cherenkov detectors (WCDs) covering an area of 22,000 m². Each WCD boasted dimensions of 7.3 meters in diameter and 5 meters in height. Despite having only a single layer of PMTs, these detectors were situated at a depth exceeding the typical path length of electromagnetic particles, resulting in them being more responsive to the secondary penetrating muons. Due to the punch-through effect of electromagnetic components, extant gamma observatories employing similar designs do not directly quantify the number of muons. Instead, they tend to rely on parameters related to the lateral distribution function (LDF), such as A4, compactness, and PINCness, for the discrimination of primary gamma rays from hadrons [10,11].

Muon detectors benefit from the strong penetrating capability of muons, enabling their shielding with substantial absorptive materials to prevent the electromagnetic component. The IceTop air shower array comprises 162 ice tanks, spaced at 125 meters intervals, each tank possessing a 1.82-meter diameter and 1.1-meter height. These tanks are further endowed with a 2-meter-depth cover of overburdened snow to attenuate electromagnetic secondaries. Consequently, the IceTop/IceCube collaboration [12] employs a statistical approach to measure muon densities at significant distances from the shower axis [13]. The Pierre Auger Observatory [14] implements a hybrid technique to ascertain the muon content within EAS. Underground muon detectors are deployed among the water-Cherenkov surface detectors, with an array of scintillator modules buried in the soil to reduce pollution by the electromagnetic content [15]. The Tibet AS γ -III+MD project [16] employs a configuration of 4500 m² underground WCDs buried under 2.5 meters of soil. This configuration facilitates the detection of EAS muon content on an event-by-event basis, thereby enhancing gamma/hadron separation capability and enabling the detection of cosmic gamma rays with energies in the hundreds of TeV range [17,18].

The LHAASO is a ground-based EAS experiment with a hybrid technique at 4410 m above sea level where the measured atmospheric depth is around 600 g/cm². At this specific atmospheric depth, secondary electrons/positrons and gamma rays surpass secondary muons by a factor of approximately one and two orders of magnitude, respectively. Consequently, the measurement of secondary muons is encumbered by a substantial contamination of electromagnetic components. Within the framework of the LHAASO experiment, the kilometer-square array (KM2 A) encompasses an area of approximately 1.2 km² and comprises 5216 electromagnetic particle detectors (EDs) and 1188 muon detectors (MDs). Each MD within KM2 A extends across 36 m² and is shielded by an overburden of 2.5 meters of soil to prevent interference from electromagnetic content originating from EAS. The threshold energy for detecting secondary muons exceeds 1 GeV, and the detectors exhibit both a detection efficiency and purity exceeding 95% [19,20]. The MDs are strategically distributed throughout KM2 A at intervals of 30 m, collectively covering an extensive area exceeding 40,000 m². This configuration empowers LHAASO to achieve a remarkable hadron rejection capability, amounting to 4×10^3 at energies surpassing 100 TeV [21], enabling LHAASO to unveil a dozen of ultrahigh-energy gamma-ray sources [22,23].

While the KM2A-MD array is an optimal detector of directly quantifying muon content, LHAASO encounters limitations due to its finite coverage ratio, approximately 4.4%, which imposes constraints on background rejection capabilities within the energy range of 10 TeV to 100 TeV. Fortunately, the Water Cherenkov Detector Array (WCDA), situated at the center of LHAASO, spans a substantial area of 78,000 m² and comprises 3120 homogeneous WCD units. Each WCD possesses dimensions of 25 m² in area and a depth of 4.4 m, incorporating either pairs of 8-inch and 1.5-inch photo-multiplier tubes (PMTs) in the first pond or pairs of 20-inch and 3-inch PMTs in the second and third ponds. With the implementation of the discrimination parameter, compactness, WCDA achieved a rejection power of 4.4×10^1 at 1 TeV

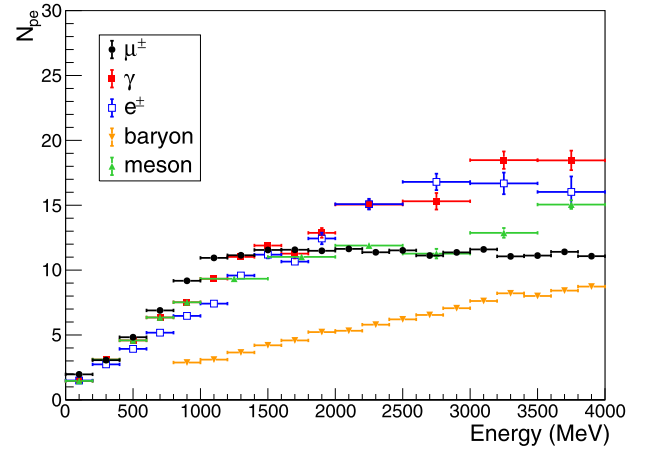


Fig. 1. Average response of a WCD with an 8-inch PMT to different EAS secondaries.

and 5×10^2 at 6 TeV individually [24]. The collective area of WCDA surpasses that of the MD array by approximately 1.8 times. While the WCDA was initially designed for gamma astronomy, it lacks absorptive materials to prevent electromagnetic secondaries. Consequently, the utilization of WCDA as muon detectors on an event-by-event basis presents substantial challenges, akin to the issues encountered by Milagro and HAWC.

This study introduces a novel method aimed at harnessing the full potential of the WCDA as a comprehensive muon counter array, specifically catering to the measurement of muon content within the domain of shower cores situated in the KM2 A area. This method facilitates event-by-event shower muon counting for the first time by utilizing unbinned WCD units. The detector responses to distinct secondary particles are elucidated in Section 2.1 via single-cell simulation. Based on this, we introduce the muon selection methodology in Section 2.2. The performance of this muon selection process is subsequently evaluated in Section 3 based on comprehensive WCDA full-array simulations. Experimental data comparisons regarding muon content in EAS between KM2A-MD and WCDA are conducted in Section 4.1. With the supplementary muon content information provided by the WCDA, the enhancement of LHAASO's gamma/hadron discrimination is explored in Section 4.2. The study culminates with our concluding remarks in Section 5.

2. Methodology

2.1. Response of a WCD to EAS secondaries

Official simulation data form the basis of this analysis, with air showers generated through the CORSIKA program [25]. Accurate simulation of the WCDA detector's response is achieved through the G4WCDA software package [26]. The validity of the simulation has been substantiated through observations of the Crab Nebula [24]. In this section, the single-cell WCD unit simulation is employed to expound upon the responses to various secondary particles. Fig. 1 shows the average response denoted as N_{pe} (the number of photo-electrons, PEs) for a WCD equipped with an 8-inch PMT in the presence of EAS secondary particles, including electromagnetic components (gamma rays, electrons/positrons), muons, and hadrons (mesons and baryons). The response pattern for a WCD outfitted with a 20-inch PMT exhibits a similar shape but with higher values of N_{pe} .

Gamma rays and electrons/positrons initiate sub-electromagnetic showers and come to stop quickly within the uppermost layer of water. The Cherenkov light produced by the secondary electrons and positrons is approximately proportional to the total energy these secondary particles deposit in the water, corresponding to the cumulative energy of

the incoming particle. This Cherenkov light is then collected by the 8-inch PMT positioned at the bottom center of a WCD unit. Consequently, a WCD functions as a calorimeter for EAS electromagnetic particles, rather than serving as a traditional scintillation detector. In specific terms, a secondary gamma ray with an energy of 1 GeV yields an average of around 10 PEs typically. Conversely, an electron/positron possessing the same energy generates roughly 7 PEs, which amounts to a 30% reduction in yield, possibly attributable to the shallower shower. To produce a single PE on the PMT, an electromagnetic particle must carry an energy of approximately 100 MeV. Consequently, secondary electromagnetic particles within EAS, typically possessing energies of around 10 MeV, yield, on average, only 0.1 PEs on the PMT. Therefore, a substantial fraction of these particles do not produce detectable Cherenkov light. The cumulative N_{pe} generated by multiple secondary particles is the summation of each component and can attain substantial values when the number of secondary particles is high, particularly in scenarios where the detector is positioned near a shower core.

An EAS muon possessing an energy below 1 GeV, which roughly corresponds to the threshold energy for a minimum ionization particle (MIP) to penetrate a WCD, exhausts its entire energy within the water medium. Consequently, this process engenders a signal with an average N_{pe} that is directly proportional to the muon's energy. The average N_{pe} exhibits a notable increase, attaining approximately 11 PEs, after which it stabilizes. This stabilization occurs because muons with energies surpassing 1 GeV can effectively penetrate the entire water medium, thereby maintaining a constant average track length within the water, irrespective of the increasing muon energy.

As for hadrons, baryons (such as a proton/antiproton or neutron/antineutron) lose energy linearly with their incident energy, but the low PE yield indicates that the water Cherenkov technique is less sensitive to baryon detection. Mesons decay rapidly with high PE yield. Given the limited presence of hadrons within the ensemble of secondary particles constituting an EAS, this analysis refrains from considering the WCD response to hadrons.

In most cases, a secondary muon with an energy exceeding 1 GeV penetrates the water within WCD units, generating a signal roughly 100 times greater than that produced by a typical electromagnetic secondary particle with an energy of around 10 MeV. This substantial disparity in signal strength enables the WCD to differentiate secondary muons from electromagnetic particles within EAS effectively. Consequently, the measurement of EAS secondary muons via WCDs becomes feasible.

Water Cherenkov tanks deployed in experiments such as KM2A-MD, Tibet ASy-MD, and IceTop/IceCube are furnished with internal reflective liners. This design ensures that the recorded N_{pe} remains closely proportional to the entire trajectory length of charged particles contained within the tank, resulting in minimal fluctuations. In contrast, WCDs exclusively capture direct Cherenkov photons emitted by incident particles in the water, rendering N_{pe} highly contingent upon the impact parameter R_p . As a muon with an energy exceeding 1 GeV penetrates a WCD, it emits Cherenkov light in the form of cones along its trajectory, as depicted in Fig. 2. The length of this trajectory, denoted as L , as “observed” by the PMT, is inversely proportional to the PMT diameter D , specifically $L \sim D/\sin \theta_c$, where θ_c represents the Cherenkov emission angle. The cumulative N_{pe} is then determined by integrating across Cherenkov photon energy, considering a light Cherenkov yield factor per unit length, dN/dE , with E representing the Cherenkov photon energy. Assuming a spherical shape for the PMT, it collects a fraction of photons ($\pi D^2/8\pi R_p D$) within the Cherenkov light cone with a radius R_p , assuming $R_p \gg D$. Accounting for light absorption within the water medium, the N_{pe} signal can be formulated as follows:

$$N_{pe} = \int_{E_0}^{E_1} \frac{D}{\sin \theta_c(E)} \cdot \frac{D}{8R_p} \cdot e^{-R_p/(\sin \theta_c(E) \cdot \lambda_{att}(E))} \cdot Q(E) \frac{dN}{dE} dE, \quad (1)$$

where the symbols $Q(E)$ and $\lambda_{att}(E)$ respectively represent the PMT quantum efficiency and the attenuation length of Cherenkov light in

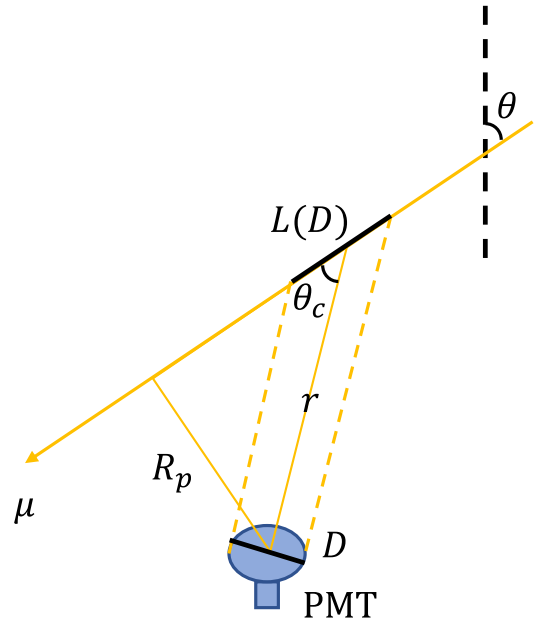


Fig. 2. The schematic of a muon trajectory that sweeps by PMT.

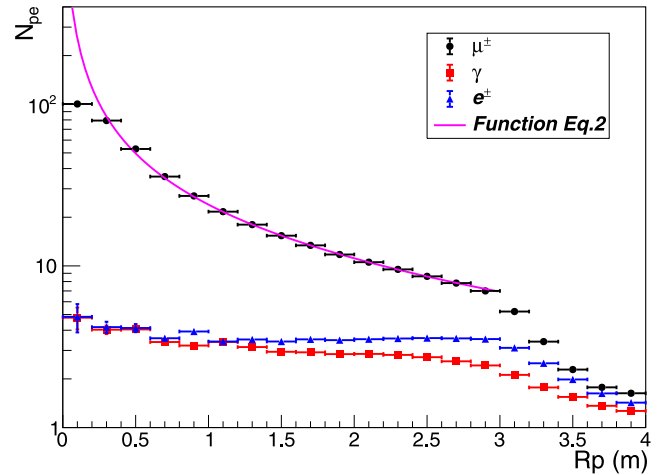


Fig. 3. The N_{pe} of EAS muons as a function of the impact parameter, R_p , from Monte Carlo simulation. The N_{pe} of electromagnetic secondaries are also plotted for reference. The fitting function based on Eq. 2 is plotted in magenta.

water. The lower and upper bounds of the incident Cherenkov photon energy are denoted as E_0 and E_1 . Notably, the proximity of the muon track to the PMT correlates with a higher recorded signal. In the absence of significant energy dependencies within these parameters, Eq. (1) can be succinctly simplified as

$$N_{pe} \propto \frac{1}{R_p} \cdot e^{-R_p/(\sin \theta_c \cdot \lambda_{att})}. \quad (2)$$

Fig. 3 presents the simulated N_{pe} values for EAS muons as a function of R_p . The simulated data align closely with the description provided by Eq. (2) (magenta curve) across a broad R_p range, spanning from 0.3 m to 3.0 m. The fitted value of λ_{att} (21.2 ± 0.4 m) derived from Eq. (2) demonstrates notable concordance with the preset value of 20 m, often considered as typical [27].

The size of the PMT should be taken into consideration at small R_p where the approximation of $R_p \gg D$ becomes invalid. Notably, for a majority of muons with $R_p > 3$ m, a segment of their trajectory extends beyond the water medium, leading to a steeper decline in N_{pe} compared

to the predictions of Eq. (2). Consequently, as muon trajectories exhibit differing R_p values, the corresponding N_{pe} values range from a few to dozens, rendering the task of muon counting based solely on WCD signal charge impractical.

2.2. Muon selection criteria

To enable the effective counting of EAS muons using WCDs, two primary challenges must be addressed. The first challenge arises from the fact that N_{pe} from an EAS muon varies greatly with its R_p . The second challenge involves the presence of punch-through contamination resulting from EAS electromagnetic particles.

Unlike KM2A-MD, WCDs operate without the protective overburden and are thus exposed to EAS secondary particles. Notably, EAS electromagnetic particles exhibit an average energy level considerably lower than that of EAS muons, leading to a notably reduced average signal generated by an electromagnetic particle in comparison to a muon. However, the total count of electromagnetic particles is typically two orders of magnitude greater than that of muons. Consequently, the collective N_{pe} produced by electromagnetic particles within an EAS is, on average, even higher than that generated by muons.

To resolve these challenges, it is imperative to focus on regions situated at considerable distances from the shower cores. In such regions, the density of electromagnetic particles is significantly diminished, resulting in only a few WCDs being triggered. Consequently, the average N_{pe} associated with each WCD remains exceedingly low. When a muon interacts with a WCD in this region, it gives rise to a substantially larger signal compared to neighboring WCDs without a muon interaction.

To apply the above conditions, it is necessary to formulate a measurable quantity to characterize the sparsity of triggered WCDs and establish a connection between this sparsity and an appropriate PE threshold. Regarding WCDs situated in an annular region at a radial distance of r from the shower axis, the trigger ratio of WCDs influenced by electromagnetic content is expressed as follows:

$$R_{\text{trig}}(r) = \frac{N_{\text{trig}}(r)}{N_{\text{total}}(r)}, \quad (3)$$

Here, $N_{\text{trig}}(r)$ signifies the count of triggered WCDs, while $N_{\text{total}}(r)$ represents the overall number of WCDs situated in the annular region at a radial distance of r from the shower axis. In regions where the number of Cherenkov photons induced by electromagnetic particles is relatively low, the N_{pe} recorded by a WCD from electromagnetic components closely conforms to a Poisson distribution, which is expressed as $P(N_{pe} = k, \widehat{N}_{pe})$. When a WCD unit remains untriggered ($N_{pe} = 0$), the expected value \widehat{N}_{pe} of this Poisson distribution can be calculated using the trigger ratio through the following equation:

$$P(N_{pe} = 0, \widehat{N}_{pe}) = 1 - R_{\text{trig}}(r). \quad (4)$$

Fig. 4 visually elucidates the interplay between the electromagnetic trigger ratio, Poisson likelihood probability, and the expected value. For instance, when $R_{\text{trig}} = 40\%$ is measured at a particular distance r_0 from the shower axis, the corresponding \widehat{N}_{pe} is determined to be 0.5 PE according to Eq. (4) (refers to the black line in Fig. 4 as well). In this scenario, a triggered WCD is most likely to register a single PE, with a likelihood probability that is four times greater than that of recording 2 PEs.

Conversely, when a WCD registers a signal considerably above \widehat{N}_{pe} , it suggests a strong likelihood that the signal originates from a muon. Consequently, it is reasonable to establish a PE threshold denoted as N_{th} , aimed at identifying WCDs as potential muon detectors based on the probability distribution of N_{pe} with given \widehat{N}_{pe} . The number of muons can be ascertained by tallying the WCDs with N_{pe} exceeding N_{th} . To ensure a reasonable level of muon selection purity amidst the prevalence of electromagnetic backgrounds characterized by small-PE hits, only those hits exhibiting N_{pe} that exceed the Poisson threshold

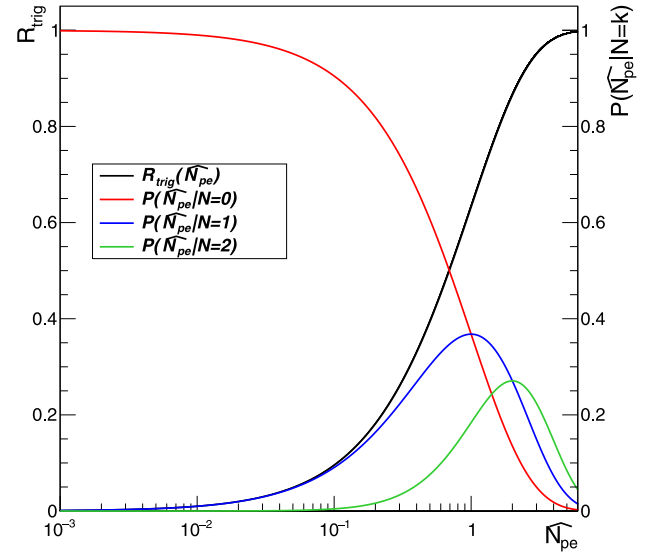


Fig. 4. R_{trig} increases with an increase in the expectation value \widehat{N}_{pe} as shown by the black line (the left-hand vertical axis). The Poisson likelihood probability $P(\widehat{N}_{pe} | N)$ of collecting N PEs from electromagnetic shower components in a WCD unit as a function of \widehat{N}_{pe} , is shown for $N = 0, 1, 2$ (the right-hand vertical axis).

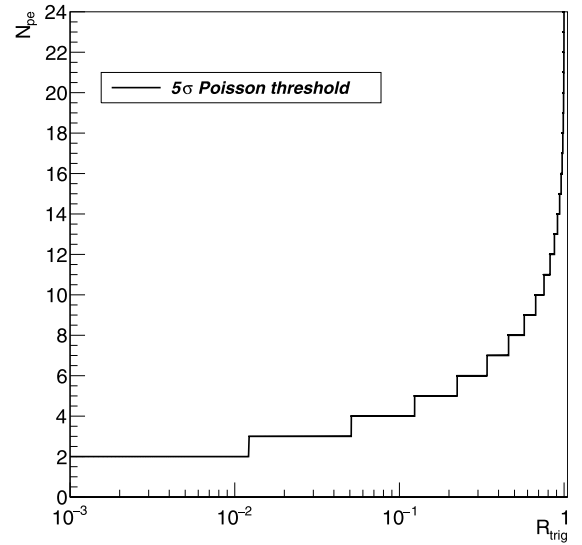


Fig. 5. The 5σ Poisson threshold for N_{pe} as a function of R_{trig} for WCD Pond 1.

by a margin of “ 5σ ” are categorized as muon-like hits. Fig. 5 provides a visual representation of the PE threshold as a function of R_{trig} . With the progressive increase in R_{trig} , the restrictiveness of N_{th} becomes more pronounced. For instance, when $R_{\text{trig}} = 40\%$, the PE threshold is set at 7 PEs.

3. Performance of the method with simulated data

3.1. Simulated datasets

The method's validity is assessed through MC simulation data as follows: Cosmic ray showers with primary energies following a power-law distribution (index of -2) in the energy range of 10 TeV to 100 TeV are simulated. These showers originate with cores situated at a distance of 80 meters from the edge of the WCDA within a square area measuring 1200 m \times 1200 m. The primary directions are uniformly sampled, with zenith angles strictly less than 20° to exclude scenarios

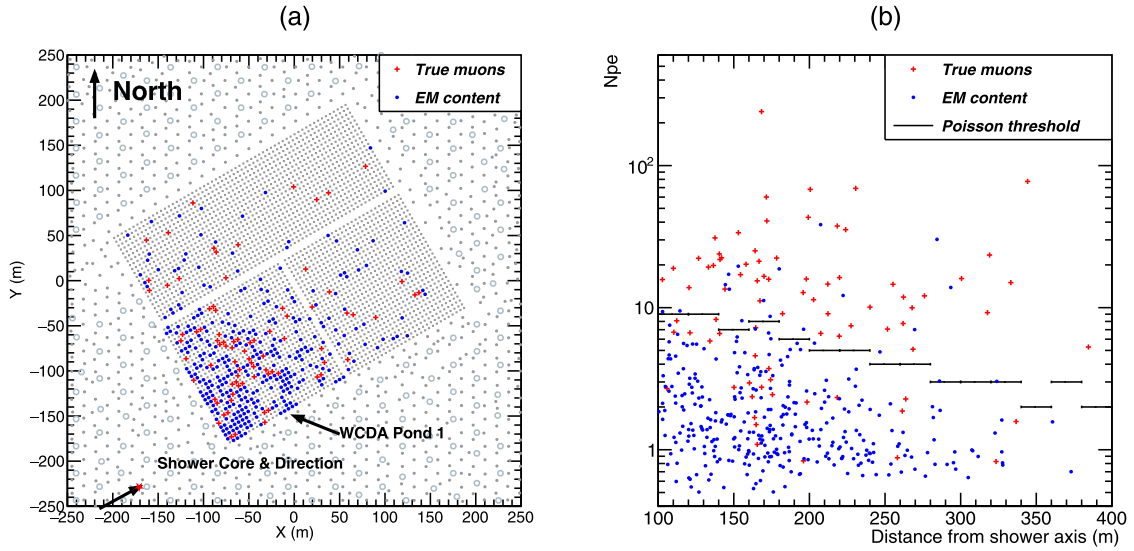


Fig. 6. A simulated shower event with a primary energy of 72.81 TeV. (a) Depicts the trigger pattern of WCD hits post-noise-filtering, labeling the different contents. A red cross signifies a WCD collecting signals from secondary muons, while a blue dot indicates a WCD collecting electromagnetic particles but devoid of muons. The red star represents the reconstructed shower core, and the black arrow delineates the shower axis in a planar view. (b) Displays N_{pe} for WCD hits relative to the distance from the shower axis. The solid lines represent the Poisson threshold applied in this particular event based on the trigger ratio.

in which shower muons with substantial zenith angles traverse multiple WCDs. Events that trigger at least 50 WCDs within 800 meters from the shower axis after noise filtering.

The trigger ratio R_{trig} is computed within a distance range starting from the shower axis, with intervals of 20 m. As the distance from the shower axis increases, both the R_{trig} and the expected value \widehat{N}_{pe} exhibit a decline. In simulated events, for those located beyond 180 m from the shower axis, where the shower cores are distant from the WCD area, the R_{trig} remains below 0.4. In such cases, the electromagnetic punch-through effect can be considered negligible since a triggered WCD is highly likely to collect just one PE based on likelihood probability. Consequently, the muon selection criteria, as mentioned in Section 2.2, for identifying muon candidate hits in the range spanning 180 m to 380 m is reliably assured.

To provide a detailed insight into our selection method, Fig. 6(a) presents the pattern of a high-energy proton shower in our simulation. The triggered WCDs with any contribution from muons are categorized as “true muon” hits, while WCDs collecting PEs without muon contribution are categorized as electromagnetic content (EM content). Due to the causality of secondary particle production, the WCD hits tend to cluster rather than being evenly distributed around the annulus. As for Fig. 6(b), each WCD hit is represented in terms of N_{pe} and its distance from the shower axis. The Poisson thresholds decrease with increasing distance from the shower axis but inevitably introduce a certain level of fluctuation based on the trigger ratio for each annulus. Furthermore, the WCD hits surpassing this threshold are chosen as muon candidate hits after applying the muon selection method, accompanied by an additional threshold of 5.0 PEs.

3.2. Muon content signature

To address these observed characteristics from a statistical perspective, the distribution of N_{pe} for the selected shower hits is presented in Fig. 7. The WCDs with any N_{pe} contribution from muons are referred to as “true muons” (N_{true}), and the WCDs selected as muon candidate hits are referred to as “selected muons” (N_{sel}). The number of WCDs that fall into both categories is denoted as “selected true muons” ($N_{true,sel}$).

The “true muon” signal exhibits a peak at several PEs. This is primarily attributed to secondary muons with energies below 1 GeV and their trajectories, which can partially interact with an 8-inch PMT. These muons represent approximately one-fourth of the “true muons”,

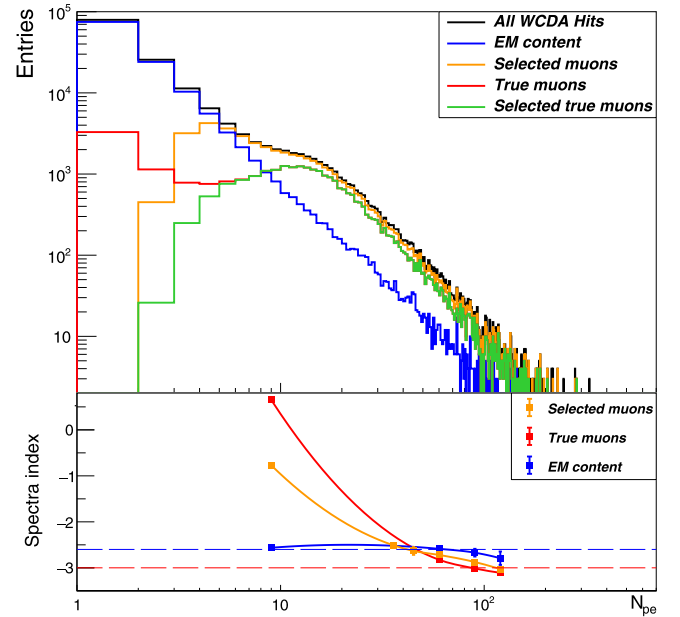


Fig. 7. The top panel displays the N_{pe} distribution from various content categories. The histograms illustrate the N_{pe} distribution for total hits (black), “EM content” (blue), “true muons” (red), “selected muons” (yellow), and events satisfying both conditions of “selected muons” and “true muons” (green). The bottom panel exhibits the power-law spectral indices of three components: “EM content” (blue), “true muons” (red), and “selected muons” (yellow). The reference power-law indices for the muon (red dashed line) and EM (blue dashed line) components are -3.0 and -2.6 , respectively.

aligning with the PMT response characteristics described in Section 2.1 and the observed pattern in Fig. 6. In contrast, the cumulative peak around 11 PEs results from the combined light yield from complete muon trajectories. The spectral index of the “true muon” signal decreases as N_{pe} increases, eventually stabilizing at a constant value of -3 . This behavior aligns with expectations and calculations considering the incidence-dependent nature of secondary muons, supporting WCD’s sensitivity to EAS muon content.

Conversely, the “EM content” signals follow a power-law distribution with an index of -2.6 , indicating that the contamination of “EM

Table 1

The efficiency, purity and effective coverage area of Muon Selection Method.

$LLLLN_{th}$ (PEs)	η_D (%)	ρ_S (%)	A_{eff} (m ²)
2.5	79.2	62.3	39,570
5.0	75.3	68.2	37,650
7.5	63.5	74.9	31,740
10.0	49.8	77.5	24,910

content” rapidly diminishes as N_{pe} increases. The “selected muons” signals begin at or above 1 PE and extend to encompass the peak signal range of muon content, typically around 10 PEs and above. Importantly, a notable distinction exists in the distribution of signals between “selected muons” and “true muons” for signals below 10 PEs. This suggests that the muon selection criteria tend to misclassify low-PE signals that lack muon contributions as muon candidate hits. Hence, the incorporation of an additional threshold is indispensable to ensure the method’s effectiveness when dealing with low-PE signals, as mentioned in Section 3.1, which includes the additional threshold of 5.0 PEs.

The spectral index of “selected muons” also decreases as N_{pe} increases. Specifically, when N_{pe} surpasses 30 PEs, the index is slightly harder than that of “true muons” but softer than that of “EM content”. This observation implies the presence of signal contamination from electromagnetic particles within the distribution of “selected muons” in high-PE signal scenarios.

3.3. Efficiency and purity

To quantitatively assess the performance of the muon selection method, the selection purity (ρ_S) is evaluated using different N_{pe} thresholds and can be expressed as:

$$\rho_S = \frac{N_{true,sel}(N_{pe} \geq N_{th})}{N_{sel}(N_{pe} \geq N_{th})}. \quad (5)$$

To characterize the sensitivity of WCDA to EAS secondary muons as a function of the PE threshold, the detection efficiency (η_D) is calculated:

$$\eta_D = \frac{N_{true,sel}(N_{pe} \geq N_{th})}{N_{true}}. \quad (6)$$

The influence of the distance from the shower axis on the efficiency and purity is examined, revealing that variations in efficiency and purity are negligible within the distance range of 180 m to 380 m from the shower axis. Consequently, the effective coverage area of WCDA as a muon counter, denoted as A_{eff} , can be estimated for a specified detection efficiency (η_D). By imposing a stricter PE threshold, this method can achieve higher purity for muon candidate selection but may introduce at least 20% contamination, as demonstrated in Table 1. This suggests that the selection method can be tailored to accommodate different efficiency and purity requirements.

The relationship between N_{sel} and N_{true} is depicted in Fig. 8. Notably, N_{sel} exhibits a slight excess over N_{true} , demonstrating a nearly linear correlation with a fitted slope factor of 0.98. This factor aligns with the expected value (the ratio of η_D to ρ_S) within the permissible margin of error. As the number of muons originating from primary cosmic rays increases, the relative discrepancy between N_{sel} and N_{true} diminishes, amounting to 11.1% at $N_{true} = 10$, 2.1% at $N_{true} = 30$, and 3.7% at $N_{true} = 50$.

4. Test of the method with experimental data

Since both KM2A-MD and WCDA are capable of simultaneously measuring muon content at the same distance from the shower axis, a comparison of the number of reconstructed muons by them serves as a valuable test of the aforementioned method. Initially, the muon density at a specific distance from the shower axis is calculated based

on the number of muons collected in MDs ($N_{\mu,MD}$). Subsequently, the expected muon number \hat{N}_μ in a WCD unit can be estimated as follows:

$$\hat{N}_\mu = \frac{N_{\mu,MD}}{A_{MD} \cdot N_{MD}} \cdot A_{WCD}, \quad (7)$$

where $A_{WCD} = 25 \text{ m}^2$ and $A_{MD} = 36 \text{ m}^2$ represent the areas of a WCD and KM2A-MD, respectively, and N_{MD} signifies the number of KM2A-MDs located in each annulus. Consequently, the expected muon number for the WCDs in this annulus is:

$$N_{\mu,KM2A} = N_{WCD} \cdot [1 - P(N_{pe} = 0, \hat{N}_\mu)], \quad (8)$$

where N_{WCD} represents the number of WCDs situated in the annulus.

4.1. Experimental datasets

Both KM2 A and WCDA commenced operations in July 2021 and March 2021, respectively. A time-matching method was employed to synchronize offline data between KM2 A and WCDA based on their respective time sequences. By comparing the reconstructed shower information between KM2 A and WCDA, the merged experimental data from KM2 A and WCDA were meticulously matched on a one-to-one basis, as illustrated in the example provided in Fig. 9. This matching process effectively eliminated any accidental coincidence background events, resulting in datasets in which recorded shower events were simultaneously measured by both KM2 A and WCDA.

The KM2 A demonstrates precise measurements of shower parameters, encompassing direction, core position, and energy [21]. For showers with a zenith angle less than 20°, the energy resolution is approximately 24% at 20 TeV and 13% at 100 TeV. The angular resolution is around 0.5° at 20 TeV and 0.24° at 100 TeV, while the reconstructed core resolution is about 4 m at 20 TeV and 2 m at 100 TeV.

As the KM2 A provides more accurate reconstructions when the shower core is within the KM2 A area, we utilize KM2A’s shower information instead of WCDA’s. To ensure precise measurements of the muon content in EAS by KM2A-MD and WCDA, we apply additional event selection criteria, consistent with the full array simulation:

- The reconstructed shower core must be located within 80 meters of the KM2A’s edge.
- The reconstructed zenith angle should be less than 20°.
- The reconstructed energy must exceed 10 TeV.
- The event must trigger at least 50 KM2A-EDs, 20 KM2A-MDs, and 50 WCDs within 800 meters from the shower axis after noise filtering.
- The number of deployed MDs and WCDs in the annulus from 180 m to 380 m should exceed 250 and 2000, respectively.
- Each triggered KM2A-MD in the annulus from 180 m to 380 m should collect fewer than two muons.

4.2. Comparison of muon content measured by KM2 A and WCDA

We conducted this comparison using data collected on September 2nd, 2021. For each event, the number of reconstructed muons by KM2A-MD and WCDA ($N_{\mu,WCD}$) was calculated. The relationship between $N_{\mu,WCD}$ and $N_{\mu,KM2A}$ exhibits a linear trend, as depicted in Fig. 10.

It is important to note that due to the finite coverage ratio of KM2A-MD, the measurement of muon content in EAS by KM2A-MD (resulting in $N_{\mu,KM2A}$) is subject to some inaccuracy and the inherent introduction of fluctuations. Furthermore, the fitting slope of 0.86 for $N_{\mu,WCD}$ and $N_{\mu,KM2A}$ suggests that the muon counting efficiency of WCDA is inferior to that of KM2A-MD, aligning with predictions from the WCDA simulation.

Emphasizing the scatter distribution above the reference line, particularly in cases where $N_{\mu,KM2A} < 50$, it becomes evident that, when

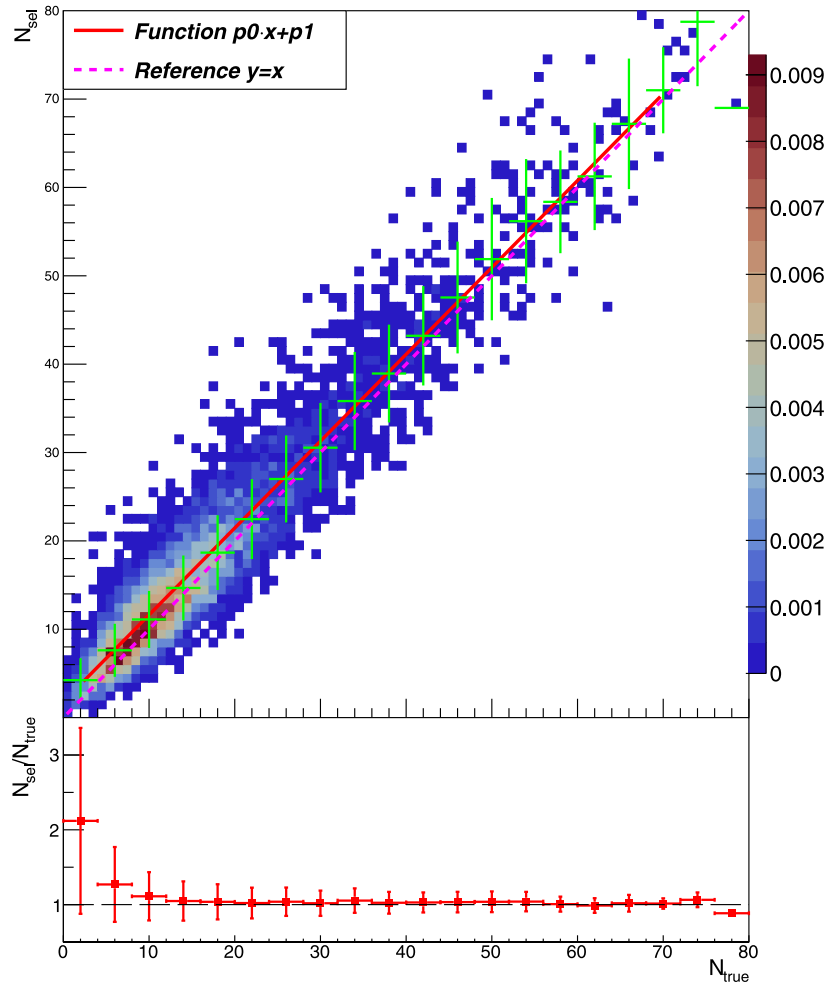


Fig. 8. The top panel illustrates the distribution of N_{sel} and N_{true} , with a threshold exceeding 5.0 PEs, in simulated proton events. Green crosses denote the 1σ standard deviation of N_{sel} . The bottom panel represents the ratio of N_{sel} to N_{true} , with the accompanying 1σ standard deviation of the ratio.

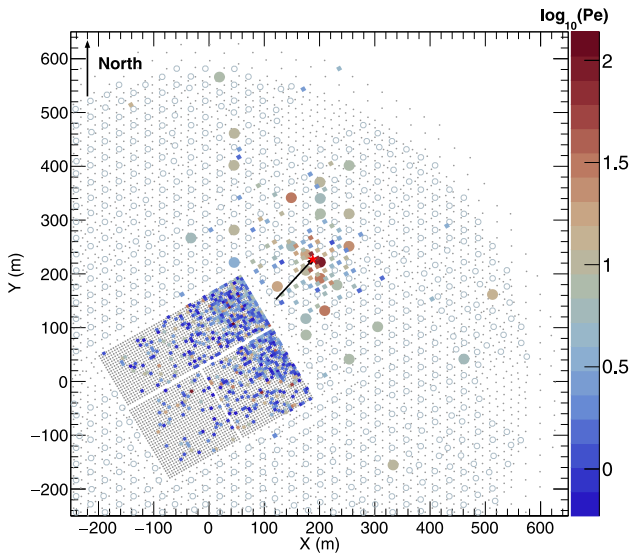


Fig. 9. A shower event was observed with reconstructed energy of 46 TeV, revealing the triggered pattern of hits from both KM2 A and WCDA following the noise-filtering process. These hits are color-coded by $\log_{10}(N_{\text{pe}})$. The rectangular region encompasses WCDA hits, while KM2 A hits are represented by large circles (KM2A-MDs) and small rectangles (KM2A-EDs). The red asterisk indicates the reconstructed shower core, and the black arrow designates the shower axis in a plane view.

taking selection purity into account, WCDA's capacity to measure the muon content is approximately equivalent to that of KM2A-MD at the same distance from the shower axis. If this method were to be implemented, LHAASO could potentially gain an additional 37,650 m² of muon-counting capability.

4.3. Exploration of further discrimination power beyond KM2A

Most of the shower events recorded by KM2 A are cosmic-ray-induced. However, due to the limited coverage of the KM2A-MDs (4.4%), KM2 A has difficulty distinguishing between gamma-ray and hadronic showers when dealing with muon-poor showers induced by cosmic rays. These cosmic-ray-induced events produce very few secondary muons, making them appear similar to gamma-induced showers to KM2 A. To assess the potential of the muon selection method in enabling the joint use of KM2 A and WCDA for improved gamma/hadron separation, we utilize a subset of these events.

The dataset spans from 20th July 2021 to 14th June 2022, totaling 330 days. We analyze data from the Crab Nebula, a “standard candle” gamma-ray source within the 10–100 TeV range, using the equi-zenith method, with most events concentrated around the median energy of 20 TeV. Thus, the OFF window events are all cosmic-ray induced while the ON window events include a considerable number of gamma rays. The event selection criteria are detailed in Section 4.1, and cosmic ray cuts for gamma/hadron discrimination align with those in [21]. The parameter used for gamma/hadron separation by KM2 A is expressed

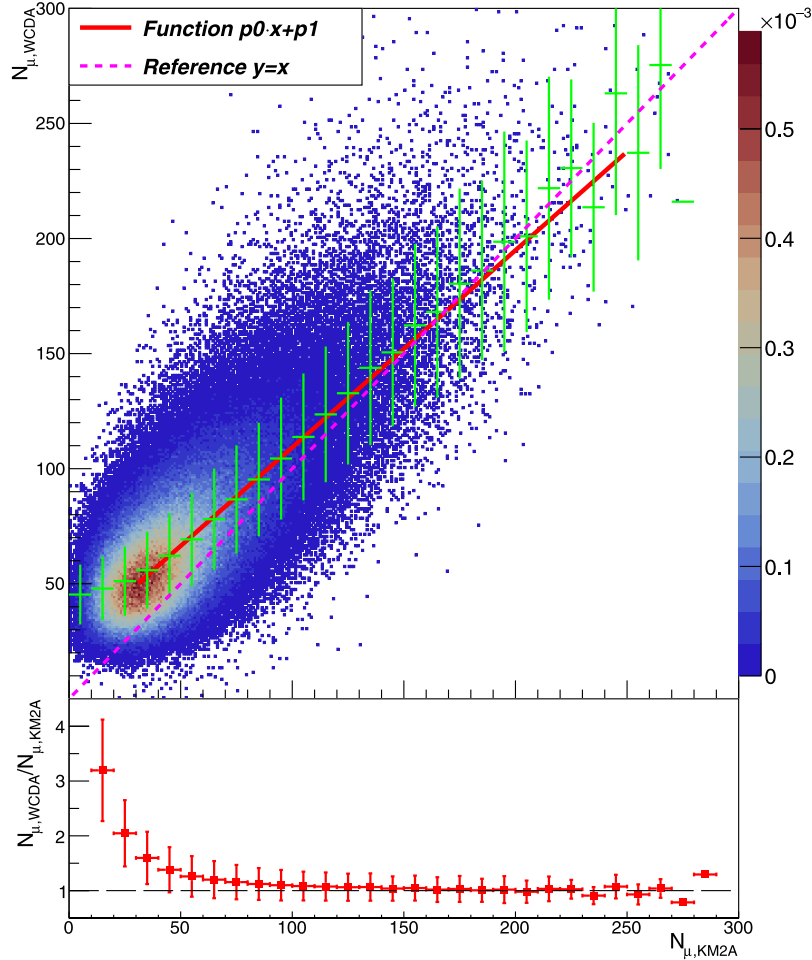


Fig. 10. The top panel displays the distribution of the number of muons measured by KM2A-MD and WCDA, with a threshold greater than 5 PEs, as a function of the number expected based on the KM2A-MD measurement. Green crosses indicate the 1σ standard deviation of $N_{\mu,WCDA}$. The bottom panel illustrates the ratio of $N_{\mu,WCDA}$ to $N_{\mu,KM2A}$, with the 1σ standard deviation of the ratio also included.

as:

$$R = \log \left(\frac{N_{\mu} + 0.0001}{N_e} \right), \quad (9)$$

where N_{μ} and N_e represent the number of muons and electrons measured by KM2A-MDs and KM2A-EDs, respectively. After applying the gamma/hadron discrimination cut by KM2 A, this process yields two distinct categories of muon-poor events: those originating from known gamma-induced events within the ON window and those originating from known CR-induced events within the OFF window.

In this situation where KM2 A has run out of rejection power in poor-muon showers, we use the reconstructed shower observables by WCDA to explore the further discrimination power beyond KM2 A. The R values are re-calculated based on the number of the reconstructed muons and electromagnetic particles by WCDA event by event and the distribution of R is plotted in Fig. 11. The discrimination parameter R yield by WCDA exhibits excellent performance in gamma/hadron discrimination, and a cut condition of $R < -1.35$ is applied. After implementing this cut, 853 out of 4885 OFF window events are retained, while 156 out of 234 ON Window events pass the selection. To quantify the improvement in rejection power, this cut effectively rejects 82.5% of cosmic ray events, with a loss of at most 33.3% of gamma events due to the absence of muon content information in EAS from KM2A-MD measurements. This corresponds to a quality factor of 1.62.

5. Conclusion

We have introduced a novel method for quantifying the muon content in EAS with LHAASO KM2A-WCDA synergy. This approach combines mathematical derivations and single-cell WCD simulations, offering a robust solution for muon selection. The theoretical efficiency and purity of the method were evaluated through WCDA simulations, confirming its feasibility and performance in accurately measuring the muon content in EAS. We adapted this method to measure the muon content in experiment data and confirmed that this method could effectively measure the muon content in EAS. A linear relationship between the number density of muons as measured by KM2A-MD and WCDA confirmed the basic hypothesis of the muon selection in WCDA. The performance of this muon selection method was verified for muon-poor showers, and the additional muon sensitivity of WCDA managed to enhance the gamma/hadron separation.

For the first time, this method utilizes an unburied water Cherenkov detector array to ascertain the muon content in each shower, effectively providing LHAASO with an additional 37,650-square-meter effective muon detection area, which is approaching the total detector area of KM2A-MD. Not only the LHAASO and other similar experiments will benefit from this method to enhance background rejection power. With the WCDA's potential to serve as a reliable muon detector, the LHAASO KM2A-WCDA synergy contributes significantly to the fields of EAS physics and gamma astronomy.

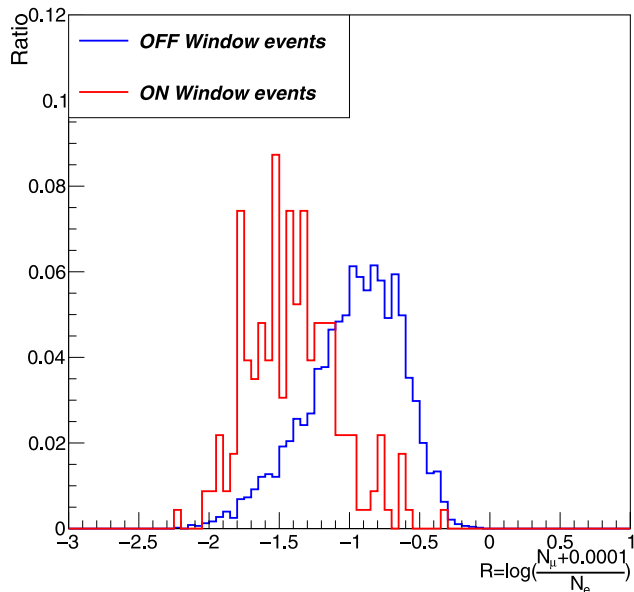


Fig. 11. The distribution of the redefined discrimination parameter by WCDA. The blue histogram represents OFF Window events, while the red histogram represents ON Window events.

Declaration of competing interest

The authors declare that they have no known competing financial interests or personal relationships that could have appeared to influence the work reported in this paper.

Data availability

Data will be made available on request.

Acknowledgments

The authors would like to thank all staff members who work at the LHAASO site above 4400 meter above the sea level year round to maintain the detector and keep the water recycling system, electricity power supply and other components of the experiment operating smoothly. We are grateful to the Chengdu Management Committee of Tianfu New Area for their constant financial support of research with LHAASO data. This work is supported in China by the National Key R&D program of China under the grant 2018YFA0404201, by the National Science Foundation of China, NSFC, (Nos. 12205314, 12022502, 12105294), by the Youth Innovation Promotion Association CAS (No. 2022010), and in Thailand by the National Science and Technology Development Agency (NSTDA) and the National Research Council of Thailand (NRCT): High-Potential Research Team Grant Program (N42A650868).

References

- [1] F. Aharonian, A. Akhperjanian, U.B. De Almeida, A. Bazer-Bachi, Y. Becherini, B. Behera, W. Benbow, K. Bernlöhr, C. Boisson, A. Bochow, et al., Energy spectrum of cosmic-ray electrons at TeV energies, *Phys. Rev. Lett.* 101 (26) (2008) 261104.
- [2] A. Archer, W. Benbow, R. Bird, R. Brose, M. Buchovecky, J. Buckley, V. Bugaev, M. Connolly, W. Cui, M. Daniel, et al., Measurement of cosmic-ray electrons at TeV energies by VERITAS, *Phys. Rev. D* 98 (6) (2018) 062004.
- [3] J. Matthews, A Heitler model of extensive air showers, *Astropart. Phys.* 22 (5–6) (2005) 387–397.
- [4] J.R. Hörandel, Cosmic rays from the knee to the second knee: 10^{14} to 10^{18} eV, *Modern Phys. Lett. A* 22 (21) (2007) 1533–1551.
- [5] A. Supanitsky, A. Etchegoyen, G. Medina-Tanco, I. Allekotte, M.G. Berisso, M.C. Medina, Underground muon counters as a tool for composition analyses, *Astropart. Phys.* 29 (6) (2008) 461–470.
- [6] K.-H. Kampert, M. Unger, Measurements of the cosmic ray composition with air shower experiments, *Astropart. Phys.* 35 (10) (2012) 660–678.
- [7] G. Sullivan, M. Collaboration, et al., Status of the Milagro Gamma ray observatory, in: *International Cosmic Ray Conference*, Vol. 7, 2001, p. 2773.
- [8] A.J. Smith, The Milagro Gamma ray observatory, in: *29th International Cosmic Ray Conference*, Vol. 10, ICRC2005, 2000, pp. 227–241.
- [9] A.J. Smith, HAWC: Design, operation, reconstruction and analysis, 2015, arXiv preprint arXiv:1508.05826.
- [10] A. Abdo, M. Collaboration, Detection of TeV Gamma-ray emission from the cygnus region of the galaxy with milagro using a new background rejection technique, in: *AIP Conference Proceedings*, Vol. 867, American Institute of Physics, 2006, pp. 199–208.
- [11] R. Alfaro, C. Alvarez, J. Álvarez, J.A. Camacho, J. Arteaga-Velázquez, D.A. Rojas, H.A. Solares, R. Babu, E. Belmont-Moreno, C. Brisbois, et al., Gamma/hadron separation with the HAWC observatory, *Nucl. Instrum. Methods Phys. Res. A* 1039 (2022) 166984.
- [12] I. Collaboration, R. Abbasi, Y. Abdou, M. Ackermann, J. Adams, J. Aguilar, M. Ahlers, D. Altmann, K. Andeen, J. Auffenberg, et al., IceTop: The surface component of IceCube, *Nucl. Instrum. Methods Phys. Res. A* 700 (2012).
- [13] R. Abbasi, M. Ackermann, J. Adams, J. Aguilar, M. Ahlers, M. Ahrens, J. Alameddine, A. Alves Jr., N. Amin, K. Andeen, et al., Density of GeV muons in air showers measured with IceTop, *Phys. Rev. D* 106 (3) (2022) 032010.
- [14] A. Aab, P. Abreu, M. Aglietta, E. Ahn, I.A. Samarai, I. Albuquerque, I. Allekotte, P. Allison, A. Almela, J.A. Castillo, et al., The pierre auger observatory upgrade-preliminary design report, 2016, arXiv preprint arXiv:1604.03637.
- [15] A. Aab, P. Abreu, M. Aglietta, J.M. Albary, I. Allekotte, A. Almela, J. Alvarez-Muñiz, R.A. Batista, G.A. Anastasi, L. Anchordoqui, et al., Calibration of the underground muon detector of the pierre auger observatory, *J. Instrum.* 16 (04) (2021) P04003.
- [16] J. Huang, L. Zhai, D. Chen, M. Shibata, Y. Katayose, Y. Zhang, J. Liu, X. Chen, X. Hu, X. Zhang, et al., Performance of the Tibet hybrid experiment (YAC-II+ Tibet-III+ MD) to measure the energy spectra of the light primary cosmic rays at energies 50–10,000 TeV, *Astropart. Phys.* 66 (2015) 18–30.
- [17] M. Amenomori, Y. Bao, X. Bi, D. Chen, T. Chen, W. Chen, X. Chen, Y. Chen, S. Cui, L. Ding, et al., First detection of photons with energy beyond 100 TeV from an astrophysical source, *Phys. Rev. Lett.* 123 (5) (2019) 051101.
- [18] M. Amenomori, Y. Bao, X. Bi, D. Chen, T. Chen, W. Chen, X. Chen, Y. Chen, S. Cui, L. Ding, et al., First detection of sub-PeV diffuse gamma rays from the galactic disk: Evidence for ubiquitous galactic cosmic rays beyond PeV energies, *Phys. Rev. Lett.* 126 (14) (2021) 141101.
- [19] Z. Cao, D. della Volpe, S. Liu, X. Bi, Y. Chen, B. Piazzoli, L. Feng, H. Jia, Z. Li, X. Ma, et al., The large high altitude air shower observatory (LHAASO) science book (2021 edition), 2019, arXiv preprint arXiv:1905.02773.
- [20] C. Li, H. He, G. Xiao, S. Feng, X. Zuo, L. Wang, Y. Zhang, X. Li, N. Cheng, S.-Z. Chen, et al., Measurement of muonic and electromagnetic components in cosmic ray air showers using LHAASO-KM2A prototype array, *Phys. Rev. D* 98 (4) (2018) 042001.
- [21] F. Aharonian, Q. An, L. Bai, Y. Bai, Y. Bao, D. Bastieri, X. Bi, Y. Bi, H. Cai, J. Cai, et al., Observation of the Crab Nebula with LHAASO-KM2A - a performance study, *Chin. Phys. C* 45 (2) (2021) 025002.
- [22] Z. Cao, F. Aharonian, Q. An, Axikegu, L. Bai, Y. Bai, Y. Bao, D. Bastieri, X. Bi, et al., Peta-electron volt gamma-ray emission from the Crab Nebula, *Science* 373 (6553) (2021) 425–430.
- [23] Z. Cao, F. Aharonian, Q. An, L. Bai, Y. Bai, Y. Bao, D. Bastieri, X. Bi, Y. Bi, H. Cai, et al., Ultrahigh-energy photons up to 1.4 petaelectronvolts from 12 γ -ray galactic sources, *Nature* 594 (7861) (2021) 33–36.
- [24] F. Aharonian, Q. An, L. Bai, Y. Bai, Y. Bao, D. Bastieri, X. Bi, Y. Bi, H. Cai, J. Cai, et al., Performance of LHAASOWCDA and observation of the Crab Nebula as a standard candle, *Chin. Phys. C* 45 (8) (2021) 085002.
- [25] D. Heck, J. Knapp, J. Capdevielle, G. Schatz, T. Thouw, et al., CORSIKA: A Monte Carlo code to simulate extensive air showers, *Report fzka* 6019 (11) (1998).
- [26] S. Agostinelli, J. Allison, K.A. Amako, J. Apostolakis, H. Araujo, P. Arce, M. Asai, D. Axen, S. Banerjee, G. Barrand, et al., GEANT4—a simulation toolkit, *Nucl. Instrum. Methods Phys. Res. A* 506 (3) (2003) 250–303.
- [27] H.-C. Li, Z.-G. Yao, C.-X. Yu, M.-J. Chen, H.-R. Wu, M. Zha, B. Gao, X.-J. Wang, J.-Y. Liu, W.-Y. Liao, et al., A method to monitor and measure the water transparency in LHAASO-WCDA using cosmic muon signals, *Chinese Phys. C* 41 (2) (2017) 026002.